ACS NANO

Cite This: ACS Nano 2019, 13, 5975−5986

www.acsnano.org

ARTICLE

Atomically Precise, Thiolated Copper−Hydride Nanoclusters as Single-Site Hydrogenation Catalysts for Ketones in Mild Conditions

Cunfa Sun,[†] Nisha Mammen,[‡] Sami Kaappa,[‡] Peng Yuan,[†] Guocheng Deng,[†] Chaowei Zhao,[†] Juanzhu Yan,[†] Sami Malola,[‡] Karoliina Honkala,[§] Hannu Häkkinen,*[,‡,§] Boon K. Teo,[†] and Nanfeng Zheng*[,†]

[†]State Key Laboratory for Physical Chemistry of Solid Surfaces, Collaborative Innovation Center of Chemistry for Energy Materials, National & Local Joint Engineering Research Center of Preparation Technology of Nanomaterials, College of Chemistry and Chemical Engineering, Xiamen University, Xiamen 361005, China

[‡]Department of Physics and [§]Department of Chemistry, Nanoscience Center, University of Jyväskylä, FI-40014 Jyväskylä, Finland

Supporting Information

ABSTRACT: **Copper−hydrides are known catalysts for several technologically important reactions such as hydrogenation of CO, hydroamination of alkenes and alkynes, and chemoselective hydrogenation of unsaturated ketones to unsaturated alcohols. Stabilizing copper-based particles by ligand chemistry to nanometer scale is an appealing route to make active catalysts with optimized material economy; however, it has been long believed that the ligand−metal interface, particularly if sulfur-containing thiols are used as stabilizing agent, may poison the catalyst. We report here a discovery of an ambient-stable thiolate-protected copper−hydride nanocluster $[Cu_{25}H_{10}(SPhCl_2)_{18}]^{3-}$ that readily catalyzes hydrogenation of ketones to alcohols in mild conditions. A full experimental and theoretical characterization of its atomic and electronic structure shows that the 10 hydrides are instrumental for the stability of the nanocluster and are in an active role being continuously consumed and replenished in the hydrogenation reaction. Density functional theory computations suggest, backed up by the experimental evidence, that the hydrogenation takes place only around a single site of the 10 hydride locations, rendering the $[Cu_{25}H_{10}(SPhCl_2)_{18}]^{3-}$ one of the first nanocatalysts whose structure and catalytic functions are characterized fully to atomic precision. Understanding of a working catalyst at the atomistic level helps to optimize its properties and provides fundamental insights into the controversial issue of how a stable, ligand-passivated, metal-containing nanocluster can be at the same time an active catalyst.**

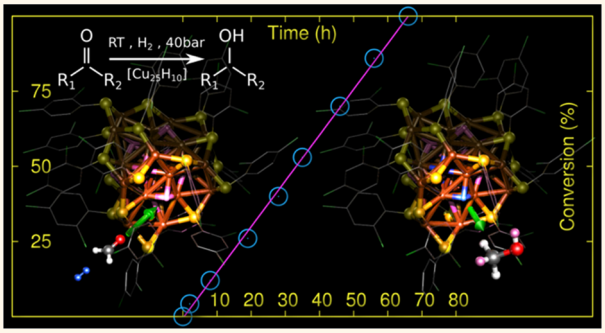

KEYWORDS: *Cu nanocluster, hydride, catalytic hydrogenation, thiolate, density functional theory, single-site catalyst*

Copper−hydride complexes have been identified to be good catalysts for several diverse organic reactions such as hydrogenation of CO, hydroamination of alkenes and alkynes, and chemoselective hydrogenation of unsaturated ketones to unsaturated alcohols;[1−3] an example of a fully characterized copper−hydride complex is $[CuH(PPh_3)]_6$, which is commercially available as Stryker's reagent.[4,5] In recent times, however, there has been tremendous interest in the use of metal nanoparticles as catalysts due to the unique electronic and catalytic properties they possess in contrast to their bulk counterparts.[6−8] In order to precisely control the stability, nuclearity, and uniform composition of these catalysts, it is desired to synthesize them as monolayer-protected clusters.[9−12]

In previous years, the composition, structure, and electronic properties of several ligand-stabilized clusters have been accurately and thoroughly investigated. In contrast to the increasing number of gold and silver nanoclusters reported in the literature,[12−21] studies on copper clusters remain relatively few.[22−24] Reported Cu nanoclusters include alkynyl-protected $Cu_{53}H_{18}$ and Cu_{20},[25,26] dithiocarbamate-protected $Cu_{28}H_{15}$ and Cu_{13},[27,28] dithiophosphate-protected $Cu_{32}H_{20}$ and $Cu_{20}H_{11}$,[29,30] and phosphine-protected $Cu_{25}H_{22}$ and Cu_6H_6.[31,32] Protected clusters with 25 noble metal atoms

Received: March 15, 2019
Accepted: May 8, 2019
Published: May 8, 2019

DOI: 10.1021/acsnano.9b02052
ACS Nano 2019, 13, 5975−5986

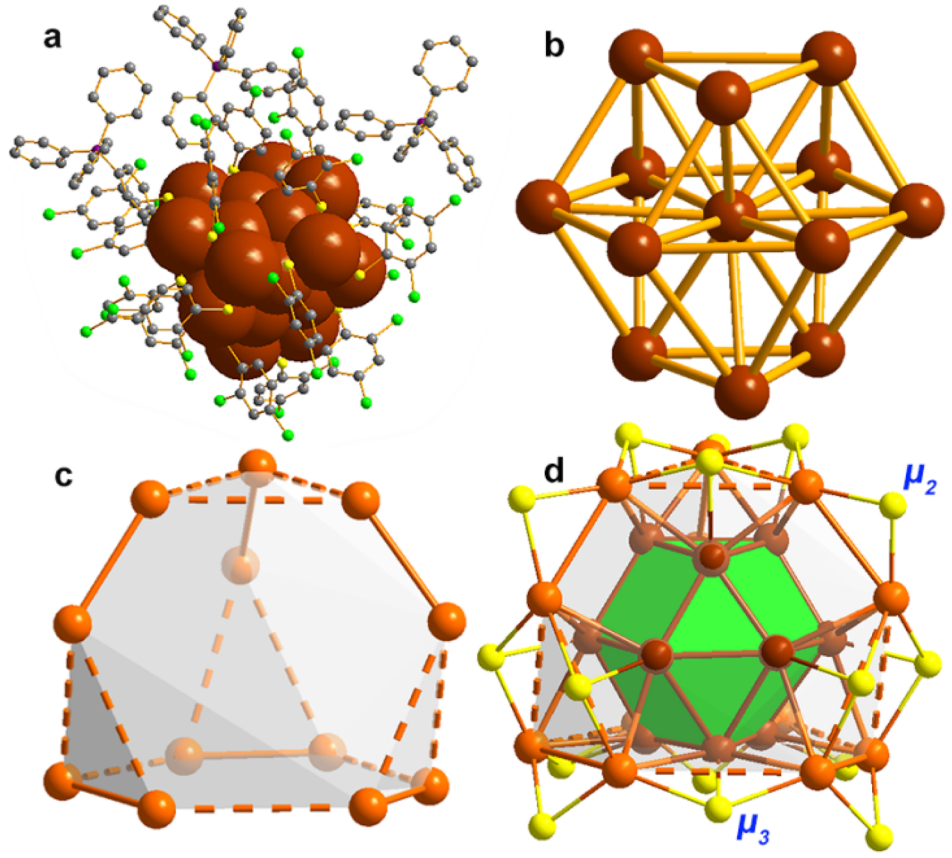

Figure 1. Structure of cluster 1 determined from X-ray diffraction results: (a) ball-and-stick view of 1 with space-filling metal core, 18 ligands ($-SPhCl_2$) and three counterions $[(PPh_4)^+]$; (b) centered twinned cuboctahedron $Cu@Cu_{12}$ inner core; (c) third layer forming a Cu_{12}-truncated v_3 tetrahedral shell; (d) metal atoms within the shell and in the two layers bridged by μ_2 and μ_3 S atoms. Color code: dark-red and light-brown, Cu; gray, C; yellow, S; bright green, Cl; purple, P. Hydrogen atoms have been omitted for clarity.

and 18 thiolate ligands, viz. $[Au_{25}(SR)_{18}]^-$ and $[Ag_{25}(SR)_{18}]^-$, have been precisely identified and studied in the past.[21,33,34] In this paper, we report the synthesis, crystallographic structure, and characterization of a thiolated copper nanocluster comprising 25 Cu atoms with 18 thiolate ligands, however, embedded with 10 hydride ions. In contrast to the Au_{25} and Ag_{25} clusters, which exist as monoanions,[21,33,34] the Cu_{25} cluster exists as a trianion, viz. $[Cu_{25}H_{10}(SPhCl_2)_{18}]^{3-}$, labeled as **1**.

Although sulfur (in thiolate ligands) has long been considered a poison for catalysis, there have been many studies reporting the catalytic activity of thiolate-stabilized clusters.[29,35] A complete atomistic picture for understanding the interaction between reactant molecules and the highly stable, supposedly chemically passivated clusters, however, has been lacking. Previous authors have suggested the activation of ligand-stabilized Au clusters by the partial removal of the protective thiolate layer, which can be achieved by suitable thermal treatment,[36] or, in the case of supported clusters, the migration of ligands from the cluster to the support.[37] In this study, we demonstrate, using a combination of experiments and first-principles calculations, that cluster **1** performs as a catalyst for the hydrogenation of ketones to corresponding alcohols at room temperature, even with all ligands perfectly intact and gain an atomistic understanding of the catalytic mechanism by a fully protected cluster.

Density functional theory (DFT) calculations predict a single-site mechanism and propose two possible energetically competing routes for the studied reaction; most interestingly, subsequent nuclear magnetic resonance (NMR) and electrospray ionization mass spectrometry (ESI-MS) experiments successfully confirm the single-site mechanism and the occurrence of one of the proposed catalytic routes. We find that the H atoms in the cluster exist as hydride ions and play a crucial role, not only in stabilizing the geometry but also in the catalytic performance of the cluster by active participation in the reaction mechanism.

A catalyst with a single reaction site is an ideal system for investigative studies as it facilitates the opportunity to determine the catalytic mechanism by means of experiments and calculations. This allows one to gain important understanding on how ligand-stabilized clusters perform as catalysts and can potentially help to offer a rational strategic principle for the design of improved catalysts.

RESULTS AND DISCUSSION

In contrast to previously reported discoveries of copper clusters, where the syntheses were carried out under deoxygenated conditions,[28,31,38,39] we carry out the synthesis of cluster **1** in air. In brief, a yellow mixture of $Cu(CH_3COO)_2$, $HSPhCl_2$, and PPh_4BPh_4 in CH_2Cl_2 is reduced by aqueous $NaBH_4$ to form the Cu nanoclusters. These clusters are then purified (by washing with a methanol solution) and crystallized from a CH_2Cl_2/hexane mixture at 4 °C, which leads to the growth of bright red crystals in the solution after about 1 week (see detailed synthesis procedure in the Methods section). The

DOI: 10.1021/acsnano.9b02052
ACS Nano 2019, 13, 5975−5986

purified product is used in all experiments to investigate the various properties of the cluster. We have divided our results here into three subsections to discuss the (i) structural properties, (ii) electronic and optical properties of cluster **1**, and (iii) the catalytic hydrogenation of ketones to alcohols.

Structural Properties of $[Cu_{25}H_{10}(SR)_{18}]^{3-}$. To examine the structure of cluster **1**, we perform a single-crystal X-ray diffraction analysis at 100 K (see Table S1 in Supporting Information for crystallographic data). This revealed that each cluster consists of 25 Cu atoms and 18 thiolates and carries a charge of −3, which is balanced by three PPh_4^+ counterions (see Figure 1a). In Figure 1b–d, we show the different atomic shells of the cluster as obtained from a detailed analysis of the crystallographic data. Figure 1b shows the Cu@Cu_{12} core that exists as a centered twinned cuboctahedron (ctco). Note the hexagonal close-packed configuration of Cu atoms in the ctco core, which is different from the cuboctahedral building block in the face-centered cubic structure of bulk Cu metal.[28,30,40] We determine the average bond distance between Cu atoms in the ctco core from both crystallographic data and the optimized geometry obtained from our subsequent DFT calculations, to be d(Cu−Cu) = 2.60 Å. We note that this value is slightly larger than that found in bulk Cu (2.56 Å) but is smaller than those reported for dithiocarbamate-protected Cu_{13} (2.64 Å) and phosphine-protected $Cu_{25}H_{22}$ (2.64 Å) clusters.[28,31] Figure 1c shows the next layer of metal atoms that forms a truncated v_3 tetrahedral (t3t) shell in such a way that each distorted hexagonal face of the shell aligns with a trigonal face of the ctco core. The Cu−Cu bond distances within the shell and between atoms in the shell and core range from 2.46 to 3.11 Å. Figure 1d shows, in addition to the Cu atoms, the positions of the S atoms of the thiolate ligands. The 18 edges of the t3t shell are bridged by 18 thiolates; the shorter Cu−Cu edges (2.87 Å < d(Cu−Cu) < 3.11 Å) are bridged by two-coordinated (μ_2) S atoms, whereas the longer edges are bridged by three-coordinated (μ_3) S atoms that form a third bond with a Cu atom of the inner ctco core.[40] It is interesting to note that the structure of cluster **1** is very different from that of $[Au_{25}(SR)_{18}]^{-1}$ and $[Ag_{25}(SR)_{18}]^{-1}$, which have an icosahedral inner core and $M_2(SR)_3$ motifs (M = Au, Ag).[21,33,34]

We also find that cluster **1** is intrinsically chiral in nature; however, it crystallizes as a racemic pair in the centrosymmetric space group $P\bar{1}$ (see Figure S1). The molecule conforms to C_3 point-group symmetry. The lowering of the molecular symmetry from the idealized C_{3v} to C_3 is a result of the twisting dispositions (either clockwise or counterclockwise) of the thiolates about the idealized three-fold axis (see Figures S2 and S3). These twisting distortions may be due to steric hindrance and van der Waals interactions between the thiolate ligands (see Figure S4).

To investigate the presence of the 10 hydrogen atoms in the core of the cluster, we synthesized a deuteride analogue of the cluster, $[Cu_{25}D_{10}(SPhCl_2)_{18}]^{3-}$, labeled as $\mathbf{1_D}$, using sodium borodeuteride ($NaBD_4$) as the reducing agent. In Figure 2a, we show the ^{2}H NMR spectra of cluster **1** and deuterated analogue $\mathbf{1_D}$, in CD_2Cl_2, measured using an 850 MHz spectrometer. This allows us to obtain signals only from D atoms in the sample. For cluster **1**, we see only one peak that corresponds to the deuterated solvent CD_2Cl_2, as the cluster itself contains no D atoms. However, for deuterated cluster $\mathbf{1_D}$, in addition to the signal from CD_2Cl_2, we see the appearance of four distinct peaks with intensity ratios of 3:3:1:3. This

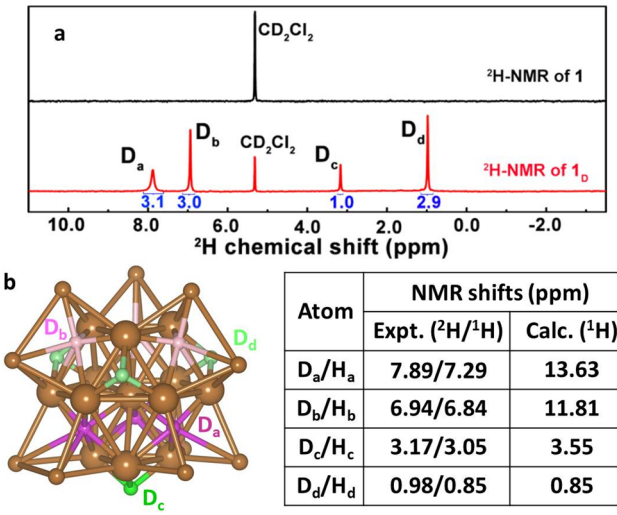

Atom	NMR shifts (ppm)	
	Expt. (^{2}H/^{1}H)	Calc. (^{1}H)
D_a/H_a	7.89/7.29	13.63
D_b/H_b	6.94/6.84	11.81
D_c/H_c	3.17/3.05	3.55
D_d/H_d	0.98/0.85	0.85

Figure 2. (a) ^{2}H NMR of cluster 1 and deuterated cluster $\mathbf{1_D}$ in CD_2Cl_2; note the four distinct peaks in the latter (intensity ratios of 3:3:1:3), confirming the presence of 10 D (or H) atoms in four different environments in the cluster. (b) Optimized geometry of the cluster obtained from DFT (ligands not shown); simulated ^{1}H NMR results listed in the table help to assign the four peaks of NMR to the four different D (or H) atoms, viz., D_a, D_b, D_c, and D_d shown in dark pink, pale pink, green, and pale green, respectively. Cu atoms are shown in brown.

strongly suggests the presence of 10 D atoms in the cluster, in four different environments, that are disposed in a three-fold symmetric arrangement, at least on the NMR time scale.

To further ascertain the presence of the 10 hydrogen atoms in the cluster, we compare the ^{1}H NMR spectra of **1** and $\mathbf{1_D}$ in Figure S5 of the Supporting Information. In both spectra, we obtain signals from H atoms in CH_2Cl_2, *n*-hexane, water, as well as H atoms in the ligand layer; however, in the spectra of **1**, we see additional peaks that are completely missing in that of $\mathbf{1_D}$. These peaks are due to the 10 H atoms in cluster **1** that are replaced by D atoms in $\mathbf{1_D}$. Additional details and analysis of the several peaks observed in the ^{1}H NMR spectra of **1** are shown in Figures S6 and S7. The experimentally determined distances between Cu−H and H−H are shown in Tables S2 and S3.

Based on a detailed analysis of the crystal structure of **1**, the Cu−Cu bond distances in the ctco core (see Figure S8) and information from previously reported structures of hydride-containing copper clusters,[30,32,40,41] we propose the positions of the 10 H (or D) atoms. These positions are validated against the peaks obtained in the difference electron density map of the crystallographic data followed by successful least-squares refinements.[23,42] Using the resolved crystal structure data from X-ray diffraction and the proposed positions for H as a starting point, we also carry out DFT calculations to further investigate the structure and stability of the cluster. Upon geometric optimization, we obtain a stable structure which is highly consistent with the experimentally proposed structure, as shown in Figure 2b. We find that the Cu−Cu bond distances in the optimized structure are in excellent agreement with those determined experimentally (see Table S4).

We also simulate ^{1}H NMR shifts for the optimized structure as listed in the table in Figure 2 (see details of the experiment in the Methods section). A clear difference can be seen in the calculated shifts of μ_3- and μ_6-H atoms; μ_3 peaks are observed

DOI: 10.1021/acsnano.9b02052
ACS Nano 2019, 13, 5975−5986

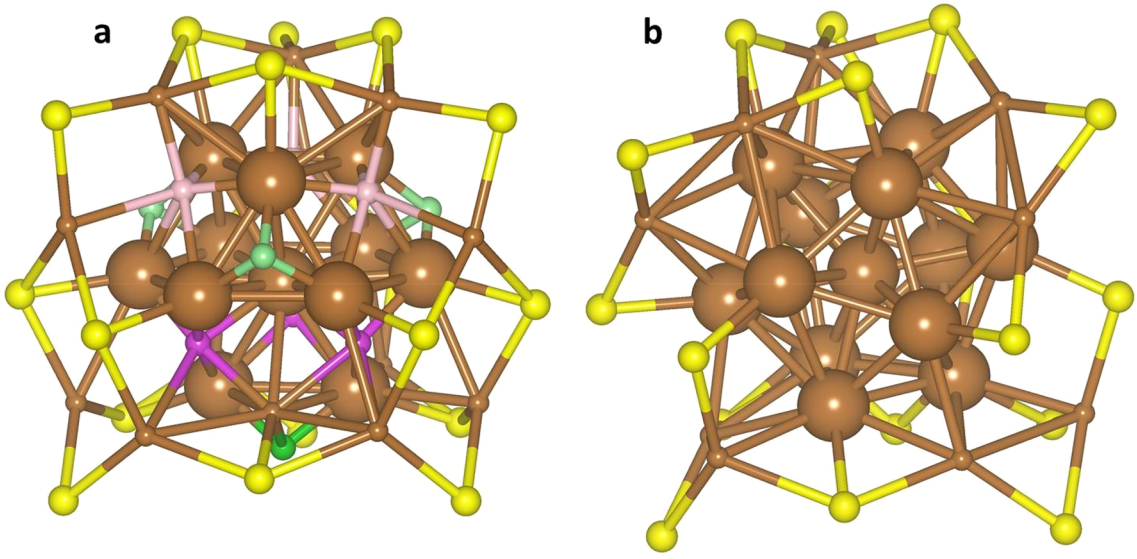

Figure 3. DFT-optimized structures omitting ligands for (a) cluster 1 and (b) H-free species. Structure in (a) was optimized directly from the experimental crystal structure, and the one in (b) was optimized after a short MD simulation. The Cu and S atoms are shown in brown and yellow, respectively, whereas H atoms are shown in dark pink, pale pink, green, and pale green. Note the loss of ctco symmetry brought about in (b) due to the removal of H atoms from cluster 1, thereby indicating the role of H in stabilizing the geometry of the cluster.

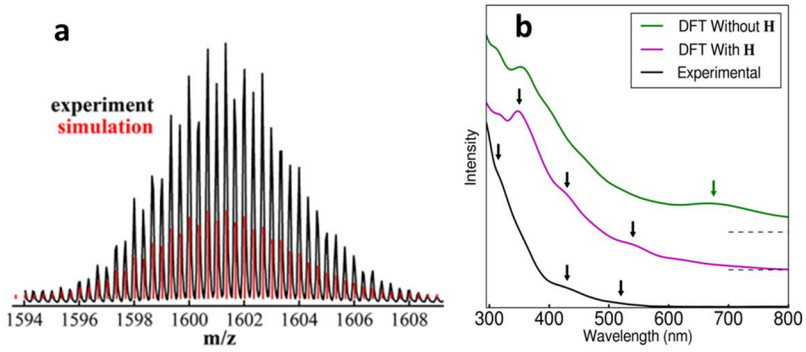

Figure 4. (a) ESI-MS measurements confirm the presence of 10 H atoms in the cluster and that it has a negative charge of −3. It matches perfectly with the simulation using the molecular formula $[Cu_{25}H_{10}(SPhCl_2)_{18}]^{3-}$. (b) Comparison of the experimental UV−visible spectra and the simulated optical spectra from DFT for cluster 1 with and without H atoms.

in the upfield region (low ppm), whereas μ_6 peaks are observed in the low-field region (high ppm) because of the differences in the shielding/deshielding conditions. We find our simulated NMR shifts to be in qualitative agreement with the spectra in Figure 2a, although the calculations overestimate the overall range of the shifts (0.85−13.63 ppm compared to the experimentally observed range of 0.85−7.39 ppm). This may be due to the missing effects of solvent and dynamics, accuracy of determining the atomic charges, and/or accuracy of describing the shielding/deshielding of nearby Cu atoms in NMR calculations. Interestingly, in agreement with the experimental NMR shifts, the calculations produce the same sequence of intensity ratios of 3:3:1:3 correlated to the symmetrically unique positions of the hydrides in the copper cage. Despite the overestimation of the observed parts per million range, the calculated shifts prove to be crucial for structural assignment; the observed NMR peaks are assigned to H positions from downfield to upfield in the following order: H_a (or D_a), H_b (or D_b), H_c (or D_c), and H_d (or D_d), as shown in Figure 2b.

The positions of the 10 hydrogen (or deuterium) atoms in the cluster are shown in Figure 2b. Six hydrogen atoms, viz. three H_a (or D_a shown by dark pink spheres in the bottom half of the cluster) and three H_b (or D_b shown by pale pink spheres in the top half of the cluster), are in six-fold-coordinated μ_6 geometries encapsulated in trigonal prismatic (tp) cages formed by the squares of the ctco core and an edge of the t3t shell. The remaining four hydrogen atoms have three-fold coordination forming a triple bridge (or a cap) over a triangle of Cu atoms; one H_c (or D_c shown by the green sphere) caps the downward-facing Cu triangle in the ctco core, and three H_d (or D_d shown by pale green spheres) cap the three Cu triangles on the top half of the ctco core. The 10 hydrogen atoms together can also be described as a trigonal prism formed by six H (H_a and H_b), with three H (H_d) capping the three square faces of the prism while the last H (H_c) caps the bottom trigonal face. Based on the structure and positions of the H atoms, it can be stipulated that the μ_6-Hs (H_a and H_b) are more interstitial in nature and may be less accessible to any reactant molecules in the environment than μ_3-Hs (H_c and H_d). We also note that H_c is in a symmetrically unique position and lies along the C_3 rotation axis of the cluster.

To understand the importance of the H to the structure of cluster **1**, we perform calculations considering a H-free species.

DOI: 10.1021/acsnano.9b02052
ACS Nano 2019, 13, 5975−5986

We consider cluster **1**, $[Cu_{25}H_{10}(SPhCl_2)_{18}]^{3-}$, and another system with the H atoms removed, $[Cu_{25}(SPhCl_2)_{18}]^{3-}$. We heat cluster **1** and the H-free species within Langevin-type molecular dynamics (MD) to a temperature of 300 K for 3.4 and 1.7 ps, respectively, by calculating the interatomic forces from DFT. In the first case, for cluster **1**, the ctco symmetry and sites of the H in the cluster are preserved during the entire simulation time, simply showing thermal vibrations. However, we find that this treatment leads to a complete collapse of the experimentally proposed cluster geometry for the second case with the H-free species: (i) the symmetry of the metal core transforms from a ctco to an icosahedral one and (ii) the Cu−Cu bond lengths obtained after subsequent geometry optimization deviate significantly from those determined from the crystallographic data (see Table S4). This reveals the important role that the hydrogen atoms play in stabilizing the structure of **1**. Figure 3a,b gives a visual representation of the optimized geometries of **1** and the hydrogen-free species, respectively.

Electronic and Optical Properties of $[Cu_{25}H_{10}(SR)_{18}]^{3-}$. ESI-MS suggests that cluster **1** is a trianionic species. We show in Figure 4a that we obtain a distinct peak in the negative ionization mode at m/z 1601.17 that can be attributed to $[Cu_{25}H_{10}(SPhCl_2)_{18}]^{3-}$ and that matches perfectly with the simulation for the molecular formula (see Figure S10 for the spectra at a larger scale). In addition, we see a peak in the positive ionization mode corresponding to the countercation $[PPh_4]^+$. This confirms that cluster **1** has a negative charge of −3 and is balanced by three countercations, $[PPh_4]^+$. It is interesting to note that this is again in contrast to $[Au_{25}(SR)_{18}]^-$ and $[Ag_{25}(SR)_{18}]^-$, both of which exist as monoanions.[21,33,34]

In Figure S11, we show our results for ESI-MS measurements on deuterated cluster $\mathbf{1}_D$, where we obtain a clear peak that corresponds to $[Cu_{25}D_{10}(SPhCl_2)_{18}]^{3-}$, once again confirming the presence of 10 D atoms in the cluster and the fact that the cluster exists as a trianion.

Using DFT, we calculate the energy required to take away an electron from cluster **1** to form the dianionic cluster, $[Cu_{25}H_{10}(SPhCl_2)_{18}]^{2-}$, to be 0.90 eV. This reinstates the finding that the cluster is stable and prefers energetically to be in a charge state of −3. By analyzing the topology of the charge density distribution in the cluster obtained from our DFT calculations, we extract charges on the different atoms using the Bader prescription,[43] as listed in Table 1. We find that the Cu atoms are positively charged; the charge on Cu increases going outward from the core to the outer shell of Cu atoms (+0.13 to +0.28 to +0.42). All H atoms are clearly negatively charged and can be described to exist as hydride ions. Here again, we see that the H_c atom behaves slightly different and is slightly more negatively charged than the rest of the H atoms. Comparing the charges on the Cu atoms in the cluster, with and without H atoms, we see that the Cu atoms are more positively charged in the presence of H atoms.

Table 1. Averaged Bader Charges in Units of Elementary Charges

atoms	average Bader charge ($\|e\|$)	
	$[Cu_{25}H_{10}(SPhCl_2)_{18}]^{3-}$	$[Cu_{25}(SPhCl_2)_{18}]^{3-}$
Cu (center atom)	+0.13	−0.06
Cu (second layer forming the ctco shell)	+0.28	+0.12
Cu (third layer forming the t3t shell)	+0.42	+0.36
S	−0.30	−0.27
H_c	−0.30	
H (H_a, H_b, H_d)	−0.26	

In Figure S12, we show the density of electronic states of cluster **1**, as obtained from DFT, which clearly shows that the cluster is nonmetallic in nature with a large energy gap of 1.64 eV. A Y_{lm} analysis of the states further reveals the absence of any "superatom-like" states of the delocalized metal electrons. 3D contour plots of the highest occupied molecular orbital (HOMO) and lowest unoccupied molecular orbital (LUMO) states are shown in Figure S13; these illustrate that the electrons bound to these states are mainly confined in the metal core but are not centrosymmetric in nature. It is interesting to note that for the H-free species $[Cu_{25}(SPhCl_2)_{18}]^{3-}$, the HOMO−LUMO gap is found to be negligible; that is, the presence of the H^- ions renders the cluster nonmetallic with a large HOMO−LUMO gap stabilizing the electronic structure. We also show in Figure S14 the cyclic voltammogram and differential pulse voltammogram data for cluster **1** in CH_2Cl_2. This shows the presence of a large electrochemical gap (about 2 eV), in accordance with the large HOMO−LUMO gap calculated from DFT.

The experimental UV−visible spectrum of cluster **1** in CH_2Cl_2, shown in Figure 4b, displays three distinguishable absorption bands at wavelengths of 315, 430 and 520 nm. This is compared to the simulated optical absorption spectra of cluster **1** (with 10 H) and the H-free species $[Cu_{25}(SPhCl_2)_{18}]^{3-}$. As can be seen in Figure 4b, the computed spectrum of cluster **1** agrees very well with the experimental spectrum showing three bands at wavelengths of 350, 430, and 540 nm. However, the computed spectrum of the H-free species shows only one major feature around the wavelength of 675 nm, which is clearly missing in the experimental data but is interestingly similar in nature to the spectra observed for $[Au_{25}(SR)_{18}]^-$ and $[Ag_{25}(SR)_{18}]^-$.[21,33,34]

Catalytic Hydrogenation of Ketones. One could naively believe that, upon protection of the cluster with ligands, the cluster should become highly stable and unreactive to any molecule in the vicinity. However, contrary to this belief, we report that cluster **1**, in the presence of the hydrides and all surface thiolate ligands, behaves as an active catalyst for the hydrogenation of ketones to alcohols. It has been well-documented that copper-based hydrogenation generally requires specific reagents such as alkalines and hydride reductants or harsh reaction conditions such as high temperatures.[44−48] Here, in contrast, we show that without introducing any reagents, cluster **1** readily catalyzes at room temperature the hydrogenation of 2-hexanone and 3-hexanone into their corresponding alcohols (see Figure 5). Note that the cluster appears to be highly stable to be able to give a constant reaction rate during the whole catalytic process (up to about 500 turnovers were tested in case of 3-hexanone).

To understand why cluster **1** behaves as a catalyst even when fully protected by thiolate ligands and to investigate the catalytic mechanism for the reaction, we resort to a combination of DFT and nudged elastic band (NEB) calculations.[49] In order to reduce the computational cost, we chose to study the catalytic hydrogenation of a model molecule, formaldehyde (HCHO), which is the smallest molecule with a C═O carbonyl bond. The thiolate ligand is also simplified from the experimental $-SPhCl_2$ to the model

DOI: 10.1021/acsnano.9b02052
ACS Nano 2019, 13, 5975−5986

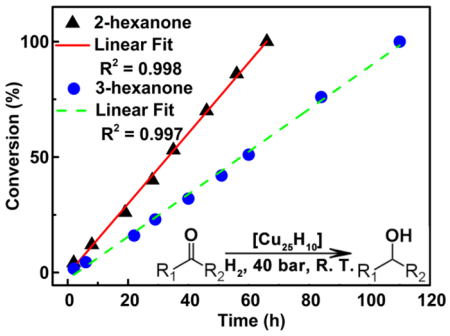

Figure 5. Hydrogenation of 2-hexanone and 3-hexanone catalyzed by cluster 1, with a turnover frequency of 7.5 and 4.5 h^{-1}, respectively. In 2-hexanone, R_1 and R_2 are $CH_3(CH_2)_3-$ and CH_3-, whereas in 3-hexanone, R_1 and R_2 are $CH_3(CH_2)_2-$ and CH_3CH_2-. Reaction conditions: 1 (1.0 μmol), hexanone (500 equiv) in solvent (15 mL) under 40 bar H_2 (see the Methods section for details).

$-SCHCl_2$. We make the choice for the model ligand based on a few simple test calculations on clusters with different ligands: −SPh, $-SCHCl_2$, and $-SCH_3$. We compare properties such as HOMO−LUMO gap, charges on the different atoms, and energy cost for removing an electron from the trianionic cluster to form a dianion (see Figure S15). Although the HOMO−LUMO gap and the charges on the Cu or H atoms do not change significantly upon changing the ligand, we find that the presence of the Cl atoms in the ligand is critical to stabilize the high −3 negative charge on the cluster. For the −SPh and $-SCH_3$ ligands, we find that the dianionic cluster is more energetically stable than the trianionic cluster. Therefore, for all further calculations to study the reactivity of the cluster, we consider the cluster with the model ligand $SCHCl_2$, viz. $[Cu_{25}H_{10}(SCHCl_2)_{18}]^{3-}$.

To begin, we study the adsorption of the reactant molecules, H_2 and HCHO, on different possible sites of the cluster. We find that the binding of molecular H_2 to the cluster is highly unfavorable; we obtain a few geometries with H_2 adsorbed on different Cu atoms; however, the binding energies of H_2 suggest that the process is highly endothermic and leads to a significant distortion in the cluster geometry. We also find that HCHO does not adsorb on the surface of the cluster as a molecule; however, it reacts with the cluster by picking up a μ_3-H atom and forms an intermediate with an alkoxy group ($-OCH_3$), viz. $[Cu_{25}H_9{-}OCH_3(SR)_{18}]^{3-}$. The C atom, which is sp^2-hybridized in the molecule HCHO, upon picking up the H from the cluster, now becomes sp^3-hybridized in the $-OCH_3$ group. Additionally, the O atom takes the place of the picked up μ_3-H and binds to three Cu atoms on the cluster. We note that because the μ_6-H atoms are more interstitial in nature than the μ_3-H, they do not interact directly with the incoming HCHO molecules. The four μ_3-Hs (*i.e.*, the H_c and three H_d) are more accessible to the molecule to be picked up to form the species with $-OCH_3$, as shown in Figure 6a−d.

We define E_b^{HCHO}, the binding energy of HCHO to the cluster as

$$E_b^{HCHO} = E\{[Cu_{25}H_9OCH_3(SCHCl_2)_{18}]^{3-}\} - E\{HCHO\} - E\{[Cu_{25}H_{10}(SCHCl_2)_{18}]^{3-}\}$$

where the three terms on the right-hand side of the equation are, respectively, the energies obtained from DFT of the intermediate with the alkoxy group, the gas phase HCHO molecule, and the cluster $[Cu_{25}H_{10}(SCHCl_2)_{18}]^{3-}$. The values of E_b^{HCHO} obtained for the different μ_3-H sites are −0.77 eV for the reaction site with H_c shown in Figure 6a and −0.34, −0.43, and −0.25 eV for the reaction sites with H_d shown in Figure 6b−d, respectively. Based on these energetics, we suggest that the reaction may proceed *via* a single-site mechanism because the H_c reaction site is significantly most preferred over the other sites. We determine the activation barrier, using NEB calculations, for the formation of the intermediate at the H_c site to be 0.72 eV. The formation and stability of the intermediate species with the alkoxy group also reveal that the hydride ions in the cluster play an important role in the catalytic process by directly interacting with the reactant molecule.

We propose that, once the intermediate $[Cu_{25}H_9{-}OCH_3(SR)_{18}]^{3-}$ is formed, the reaction can proceed *via* two possible routes: Route 1 and Route 2, as shown in Figure 7. In Route 1, we suggest that a molecular H_2 dissociates heterolytically into H^+ and H^-, close to the Cu−O bond: H^+ binds to O, forming the reaction product, the alcohol, whereas the H^- binds to the three Cu atoms and takes the position at

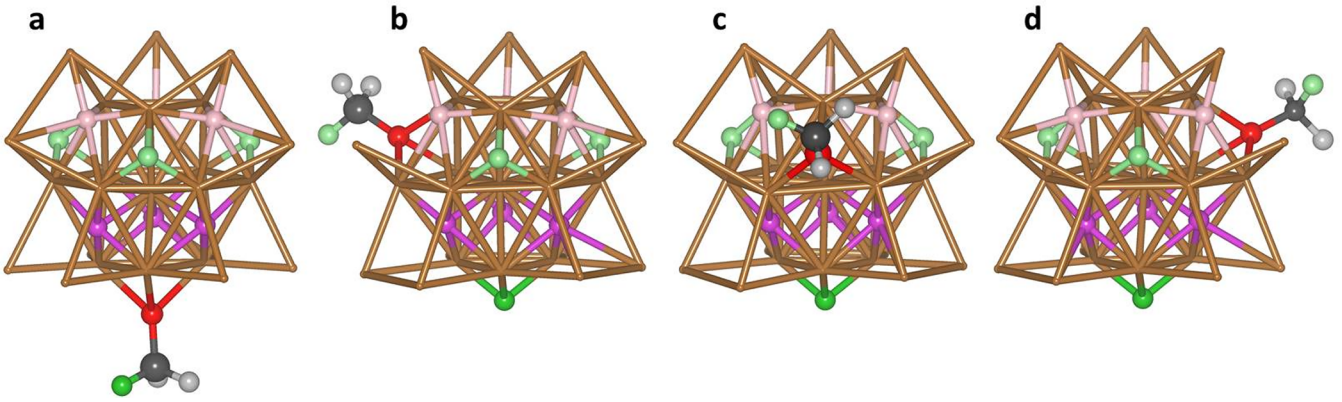

Figure 6. HCHO reacts with the $[Cu_{25}H_{10}(SCHCl_2)_{18}]^{3-}$ cluster by picking up a μ_3-H and forms an intermediate with an alkoxy ($-OCH_3$) group. In (a), HCHO interacts with the H_c atom (green sphere) at the bottom of the cluster, and in (b−d), HCHO interacts with the H_d atoms (pale green spheres) in the top half of the cluster. The frame of the Cu cluster is drawn in brown, and the hydrogen atoms H_a and H_b are shown as dark pink and pale pink spheres, respectively. The H, C, and O in HCHO are shown as light gray, dark gray, and red spheres, respectively.

DOI: 10.1021/acsnano.9b02052
ACS Nano 2019, 13, 5975−5986

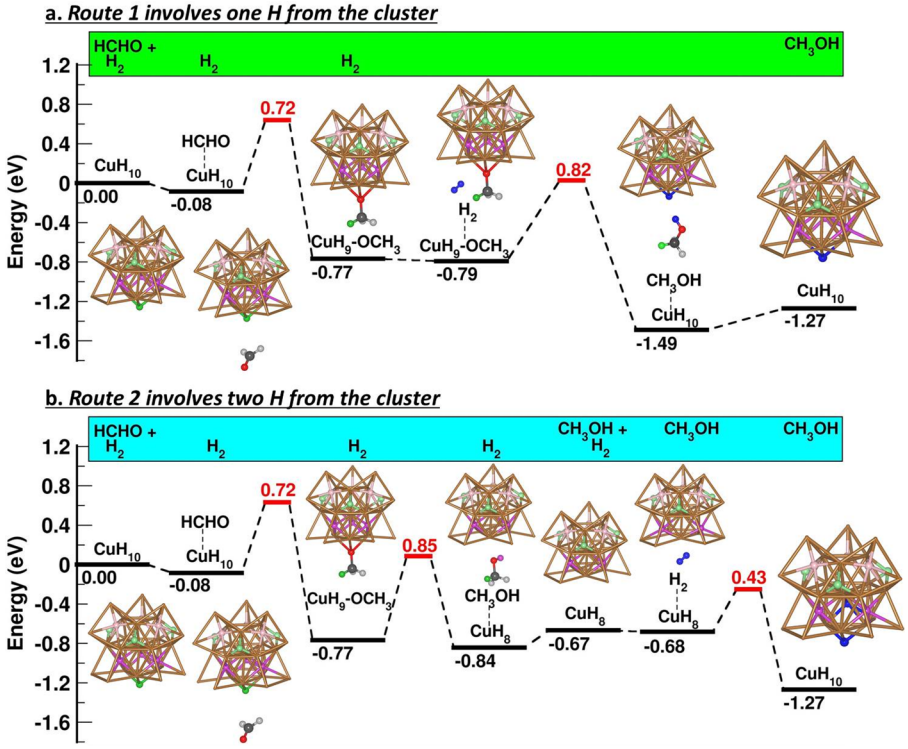

Figure 7. Energy profiles of Route 1 and Route 2 for the catalytic hydrogenation of HCHO by $[Cu_{25}H_{10}(SCHCl_2)_{18}]^{3-}$. Though not explicitly mentioned, note that all of the systems studied have 25 Cu atoms and 18 thiolate ligands. The color scheme for the atoms is the same as that in Figure 6, and H atoms in H_2 are colored blue. The numbers in black are the energies of the different states along the catalytic pathways, relative to the sum of the total energies of the isolated cluster, HCHO and H_2 in gas phase, whereas the numbers in red are the barrier heights for the forward reaction for individual steps. The gas-phase species in every elementary step are shown in the green and blue boxes for Routes 1 and 2, respectively.

the H_c site in the cluster. The barrier for this step is calculated to be 0.82 eV. The heterolytic dissociation is evidenced by the Bader charges on the H atoms of the activated H_2 molecule [d(H−H) = 0.9 Å] in the transition state of the reaction step: one H has a charge of +0.26e, whereas the other has a charge of −0.30e. The alcohol formed is weakly bound to the cluster *via* dipole−dipole interactions between the −OH group in the alcohol and the ligands in the cluster, with a binding strength of −0.22 eV with respect to the isolated cluster and gas-phase alcohol molecule. Note that, in Route 1, only one H (H_c) from the cluster participates in the reaction and is finally replaced by the H from molecular H_2, or as can be seen in the first panel of Figure 7, the green H_c atom is replaced by a blue H atom from molecular H_2 at the end of the reaction.

In Route 2, we suggest that a second H from the cluster, a neighboring μ_6-H such as H_a (shown in dark pink), may diffuse close to the O atom to form the reaction product (the alcohol), leaving behind a cluster with two H vacancies, $[Cu_{25}H_8(SR)_{18}]^{3-}$. The barrier for this process is determined to be 0.85 eV. The energy cost to create the cluster with two H vacancies from the original cluster can be calculated as $E\{[Cu_{25}H_8(SR)_{18}]^{3-}\} + E\{H_2\} - E\{[Cu_{25}H_{10}(SR)_{18}]^{3-}\}$ = +0.60 eV. The two vacancy sites are then replenished by the dissociation of molecular H_2 to complete the catalytic cycle; this step has a barrier of 0.43 eV. Note that, in Route 2, two H atoms (H_c and H_a) from the cluster participate in the reaction and are finally replaced by two H atoms from molecular H_2, or as can be seen in the second panel of Figure 7, the green H_c atom and one dark pink H_a atom are replaced by two blue H atoms from molecular H_2 at the end of the reaction.

Based on our DFT results, we suggest that the H_c site on the cluster is the energetically most preferred reaction site for the binding of molecules with a carbonyl (C═O) group. The C in the C═O group picks up the H_c atom, whereas the O binds to the three Cu atoms and takes the position of the missing H_c. Based on DFT and NEB results, we propose two catalytic pathways that are thermodynamically possible. The kinetics for the two pathways (*i.e.*, the barrier heights for the different steps along the pathways) seem to be comparable and do not favor one over the other.

Further experiments were carried out to explore the catalytic mechanism for the studied reaction and, most importantly, to validate the predictions made by our DFT calculations. In Figure 8, we show the ^{2}H NMR spectra of deuterated cluster $\mathbf{1}_D$ in the presence of the reactant molecule, 3-hexanone in CD_2Cl_2. Recall that in Figure 2a the ^{2}H NMR spectra of cluster $\mathbf{1}_D$ in CD_2Cl_2 showed, in addition to the peak for CD_2Cl_2, four distinct peaks that correspond to the four kinds of D atoms in the cluster, viz., D_a, D_b, D_c, and D_d. In Figure 8, due to the presence of the 3-hexanone molecule, we see a clear split in the chemical shift in the peak that corresponds to the hydride D_c. We believe that this clearly suggests an interaction between the reactant molecule and the D_c (or H_c) atom in the cluster; this may be an indication toward a single-site mechanism with D_c (or H_c) as the most reactive site.

To investigate and test the predicted catalytic routes, we have carried out the hydrogenation reaction in two modes: (i) $\mathbf{1}_D$ + hexanone + H_2 and (ii) **1** + hexanone + D_2. In the first case, deuterated cluster $\mathbf{1}_D$ behaves as the catalyst for the reaction between hexanone and molecular H_2. The ESI-MS

DOI: 10.1021/acsnano.9b02052
ACS Nano 2019, 13, 5975−5986

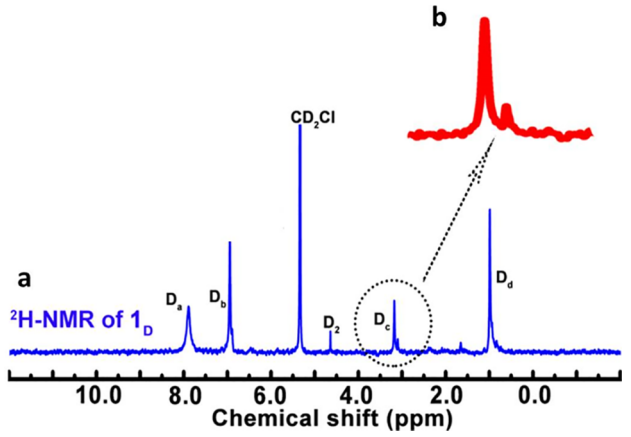

Figure 8. ^{2}H NMR of $\mathbf{1}_D$ with 3-hexanone in CH_2Cl_2. The interaction of the reactant molecule 3-hexanone with the $\mathbf{1}_D$ cluster may be causing a chemical shift in the NMR peak for D_c. This seems to support our suggestion of a single-site mechanism for the catalytic reaction.

spectrum of $\mathbf{1}_D$ after the catalytic reaction with H_2 is shown in Figure 9a. The peak obtained at m/z 2575.63 in the negative ionization mode is found to match well with the simulation for the molecular formula $[Cu_{25}D_8H_2(SPhCl_2)_{18}(PPh_4)]^{2-}$. This tells us that (at least) two D atoms from $\mathbf{1}_D$ have been replaced by two H atoms; that is, the result seems to promote catalytic Route 2. We also note the slight asymmetry of the mass peak in Figure 9a; this may indicate that 2−4 D atoms have been replaced by H as the clusters have undergone several reaction cycles. In Figure 9b, we show the ^{2}H NMR spectra of $\mathbf{1}_D$ after the catalytic reaction with H_2. This should be compared to Figure 9c (the ^{2}H NMR spectra of $\mathbf{1}_D$ before catalysis), where we see, in addition to the peak for CD_2Cl_2, four peaks in the ratio of 3:3:1:3. We see that, after the catalytic reaction, the peak corresponding to D_c has completely disappeared, which suggests that (at least) the D_c atom has definitely been replaced by a H atom. This clearly validates our prediction for the single-site mechanism with D_c being the most reactive site. Whether or not a second D atom (D_a) is missing in the cluster is difficult to infer from this ^{2}H NMR spectra.

We also carry out an experiment using cluster **1** as the catalyst for hydrogenation of hexanone with molecular D_2. Note that the ^{2}H NMR of cluster **1** in CD_2Cl_2 before catalysis (see Figure 2a) shows only one peak that corresponds to CD_2Cl_2, as the cluster itself contains no D atoms. However, the ^{2}H NMR of the cluster after catalysis with D_2 in Figure 10a shows the appearance of two new peaks, in addition to the expected two peaks from CD_2Cl_2 and molecular D_2. These two new peaks may be due to the replacement of two H atoms (in positions H_c and H_a) by D atoms in the cluster, although they do seem to be slightly shifted to upfield with respect to the D_a and D_c peaks in Figure 9c. The ^{2}H NMR of the alcohol formed is shown in Figure 10b; it shows that the product is deuterated with two D atoms. These results suggest that the Route 2 catalytic mechanism may be the preferred pathway for the reaction, as clearly two hydrogen atoms from the cluster are replaced. The fact that the product is deuterated may be due to multiple catalytic cycles performed by the same cluster; in the first cycle, two H atoms are replaced by two D atoms, and in subsequent cycles, the same two D atoms interact with the hexanone molecules to give deuterated products, to be replenished again by D atoms from D_2.

It seems to be clear now, from our DFT calculations as well as experimental data, that (i) the cluster $[Cu_{25}H_{10}(SR)_{18}]^{3-}$ behaves as a catalyst for the hydrogenation of ketones (or aldehydes) *via* a single-site mechanism with the H_c site on the cluster being the most reactive site, and (ii) the catalytic pathway proceeds *via* the mechanism "Route 2" rather than "Route 1". To understand these findings, we analyze the solvent-accessible surface area (SASA) or free space around the 10 H atoms (or 10 pockets) in the cluster $[Cu_{25}H_{10}(SCHCl_2)_{18}]^{3-}$, using the Visual Molecular Dynamics software.[50] By this method, one can measure the accessibility or the ease with which an incoming reactant molecule can approach and pick up a H from the cluster. In Figure 11a, we plot our results for the SASA values around the 10 different H sites in the cluster as a function of the radius of the probe spheres. At the onset, it is clear that, as expected, the μ_6-H (H_a

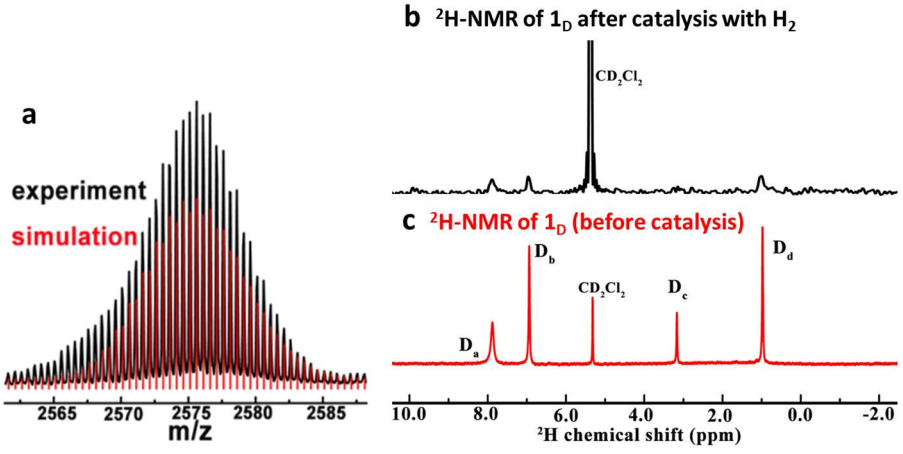

Figure 9. Reaction of $\mathbf{1}_D$ with ketone and H_2. (a) ESI-MS spectrum of re-collected $\mathbf{1}_D$ after the catalysis under H_2 shows that two to four D atoms from the cluster have been replaced by two H atoms {simulation is for $[Cu_{25}D_8H_2(SPhCl_2)_{18}(PPh_4)]^{2-}$}, which suggests the occurrence of Route 2 mechanism. (b) ^{2}H NMR spectra of $\mathbf{1}_D$ after catalysis with H_2 can be compared with (c) spectra of $\mathbf{1}_D$ before catalysis to highlight the disappearance of the D_c peak in (b); this clearly confirms our suggestion for a single-site mechanism. The D_c atom has definitely been replaced by a hydrogen atom during the catalytic process.

DOI: 10.1021/acsnano.9b02052
ACS Nano 2019, 13, 5975−5986

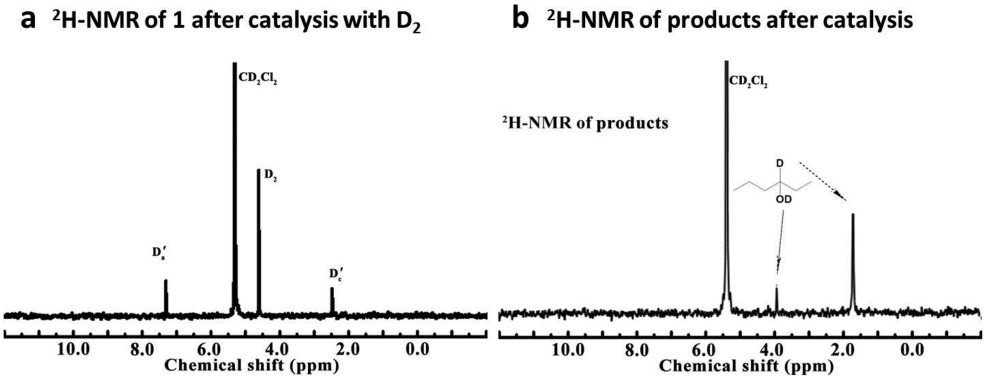

Figure 10. Reaction of 1 with ketone and D_2. (a) ^2H NMR of 1 after catalysis with D_2 shows the appearance of two peaks that may be slightly right-shifted but correspond to D_c and D_a atoms in the cluster. This confirms that two H atoms in the cluster have been replaced by two D atoms from molecular D_2, supporting the Route 2 catalytic mechanism. (b) ^2H NMR show that the alcohol product is deuterated.

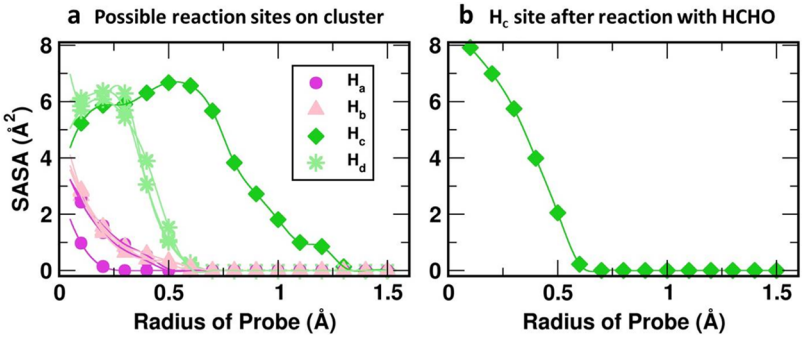

Figure 11. (a) SASA analysis of the different H sites on the cluster $[Cu_{25}H_{10}(SCHCl_2)_{18}]^{3-}$ shows that clearly μ_3-H sites (H_c and H_d) are more accessible than μ_6-H sites (H_a and H_b), and the H_c site is most accessible among the μ_3-H sites. This explains why the catalysis proceeds *via* a single-site mechanism. (b) SASA analysis of the H_c site after the formation of the intermediate with the alkoxy group ($-OCH_3$) suggests that the site is no longer very accessible even for an incoming H_2 molecule to allow the Route 1 mechanism. This explains why Route 2 may be the preferred catalytic mechanism.

and H_b) are barely accessible, or the μ_3-H (H_c and H_d) are more accessible than μ_6-H. Interestingly, we find that the H_c site is most accessible among the four μ_3-H. The H_c atom is accessible to molecules with a maximum radius of 1.3 Å; however, the H_d atoms are accessible only to molecules with a maximum radius of 0.6 Å; this may be due to the unique position that the H_c atom holds in the cluster geometry. This may explain why the catalytic reaction proceeds *via* a single-site mechanism.

In Figure 11b, we show the SASA values for the H_c pocket in the cluster after the formation of the intermediate with the alkoxy (OCH_3) group, as a function of the probe sphere radius. We now see that the H_c pocket is no longer accessible for molecules with a radius greater than 0.6 Å. Note that this analysis was carried out using the cluster with model ligands and model reactant molecule HCHO. In the real scenario, the presence of the experimental ligands and the hexanoxy group may reduce the accessibility of the pocket even further; that is, the site may no longer be accessible for a H_2 molecule to dissociate close to the Cu−O interface to allow the Route 1 mechanism. This may be the reason why Route 2 is the preferred catalytic mechanism for the reaction.

CONCLUSIONS

In this work, we have synthesized and fully characterized an ambient-stable, atomically precise, thiolated $Cu_{25}H_{10}$ nanocluster by experimental and computational methods and showed that this cluster is an active catalyst for hydrogenation of ketones to corresponding alcohols in mild conditions. The 10 hydrogens found inside the copper core are in hydride form and play a crucial role in stabilizing the structure and acting as a hydrogen source in the catalytic reaction. Density functional theory computations predict a single-site mechanism that is confirmed by experimental data. Although the activity of the $Cu_{25}H_{10}$ cluster is below that of a typical industrial catalyst, this system offers important insight into understanding catalytic reactions at the atomistic level and at the same time sheds light on the controversial issue of how a ligand-protected metal cluster can have a catalytic function.

METHODS

Reagents. Copper(II) acetate monohydrate [$Cu(CH_3COO)_2 \cdot H_2O$, purity 99%], sodium borohydride ($NaBH_4$, purity 98%), sodium borodeuteride ($NaBD_4$, purity 99%), dichloromethane (CH_2Cl_2, A.R.), and methanol (CH_3OH, A.R.) were purchased from Sinopharm Chemical Reagent Co. Ltd. (Shanghai, China). Tetraphenylphosphonium tetraphenylborate (TPPTPB, purity 99%), 2,4-dichlorobenzenethiol ($HSPhCl_2$, purity 99%), 2-hexanone (purity 99%), and 3-hexanone (purity 99%) were purchased from Alfa Aesar Chemical Reagent Co. Ltd. (Tianjin, China). The water used in all experiments was ultrapure. All reagents were used as received without further purification.

Synthesis of $[Cu_{25}H_{10}(SPhCl_2)_{18}][PPh_4]_3$ (1). In a typical synthesis, 100 mg of $Cu(OAc)_2 \cdot H_2O$ and 32 mg of TPPTPB were dissolved in a mixed solvent of 2 mL of methanol and 4 mL of CH_2Cl_2, followed by the addition of 30 μL of $HSPhCl_2$ under vigorous stirring. After 20 min, 3 mL of an aqueous solution of

DOI: 10.1021/acsnano.9b02052
ACS Nano 2019, 13, 5975−5986

$NaBH_4$ (30 mg/mL) was added dropwise to the reaction mixture. After being aged for 3 h at 25 °C, the aqueous phase and precipitate were removed, whereas the organic phase was concentrated and washed with MeOH/H_2O (4:1 by volume) several times and then dissolved in CH_2Cl_2 for further analysis. By diffusion with hexane at 4 °C for 1 week, bright-red single crystals suitable for X-ray diffraction study were obtained with 18% yield based on copper. With the same procedures, instead of $NaBH_4$, $NaBD_4$ was used to synthesize the deuterium analogue ($\mathbf{1}_D$).

Single-Crystal Analysis. The diffraction data of all compounds were collected on an Agilent Technologies SuperNova system and an X-ray single-crystal diffractometer with Cu Kα radiation (λ = 1.54184 Å) at 100 K. The data were processed using CrysAlis^{Pro}.[51] All structures were solved and refined using full-matrix least-squares based on F^2 with ShelXT and ShelXLwithin Olex2 programs.[52−54]

Hydrogenation of Ketone. A total of 0.1 μmol of **1** and 50 μmol of 2-hexanone or 3-hexanone was dissolved in CH_2Cl_2 within a well-stirred autoclave. Once sealed, the autoclave was purged three times with hydrogen and then pressurized to 40 bar. The reaction was then allowed to proceed, and samples were withdrawn at regular intervals, filtered, and analyzed to monitor product distribution by gas chromatography. The analysis was performed with a FuLi 9790II gas chromatograph, equipped with a split/splitless injector, a capillary column (KB-5, 30 m × 0.32 mm × 0.33 μm), and a flame ionization detector. Clusters **1** and $\mathbf{1}_D$ were re-collected from the solution for further study.

Measurements of Optical Properties. Pure crystals were dissolved in Spectro-grade CH_2Cl_2 for spectrum measurements. UV/vis absorption spectra were recorded on a Varian Cary 5000 spectrophotometer using a quartz cuvette of 1 mm path length. The signal of the blank solvent was subtracted. For each spectrum, eight scans at a scanning speed 100 nm/min with a data pitch of 0.1 nm were averaged. The spectra were recorded at room temperature.

Measurements of H NMR. ^{1}H NMR and ^{2}H NMR spectra were recorded on an AVANCE III 850 MHz spectrometer in dichloromethane-d_2 and dichloromethane, respectively. Chemical shifts are reported in parts per million with the internal TMS signal at 0.0 ppm as a standard.

Electrochemical Test. All of the electrochemical measurements were operated at room temperature in a three-electrode system on a potentiostat (CHI760E) under N_2. A glass carbon electrode ($\pi \times (0.2)^2$ cm^2) was selected as the working electrode, and the Pt electrode (1 × 1 cm^2) and saturated calomel electrode served as the counter and reference electrodes, respectively.

Computational Details. The density functional theory was implemented as in the GPAW package.[55] All of the calculations were done in a real space grid with a grid spacing of 0.20 Å. The exchange and correlation effects were modeled using the PBE (Perdew−Burke−Ernzerhof) functional.[56] The initial structure for relaxation was obtained directly from the crystallographic data. The cluster was set in a computational cell with 6 Å of vacuum around the cluster. As the counterions were removed from the DFT calculations, the total charge of the system was set to 3−. The structures were optimized by using a maximum residual force criterion of 0.05 eV/Å. The Bader charge analysis[43] was run on the total DFT electron density. The superatomic nature of the clusters was studied with Y_{lm} analysis by projecting the electron states to spherical harmonics centered to the center of mass.[57]

The optical response of the clusters was simulated in the linear-response time-dependent DFT scheme with local density approximation, as implemented in GPAW.[58] The transitions were considered up to 4.4 eV.

The molecular dynamics simulations were run using Langevin dynamics with a target temperature of 300 K, a friction parameter of 0.01 fs^{-1}, and a time step of 2 fs. The masses of all hydrogen atoms were increased to the mass of deuterium to allow for the longer time step.

NMR shifts were calculated using the gauge-including projector-augmented wave formalism as implemented in pseudopotential and planewave-based DFT code package Quantum ESPRESSO.[59] We used ultrasoft pseudopotentials (http://www.quantum-espresso.org/pseudopotentials), kinetic energy cutoff of 680 eV for wave functions, and energy cutoff of 6800 eV for the charge density. The shifts were calculated for the structure optimized with a PBE functional using total charge of 3−. Total chemical shifts of atoms were defined as $\sigma = \sigma(\text{ref}) - \sigma(\text{calc})$, where σ(ref) was fixed to 28.00 ppm. With the chosen reference, the most upfield ^{1}H NMR signal of the hydrides inside the metal core will be reproduced in calculations (0.85 ppm; see table in Figure 2).

The activation barriers for the elementary steps in the catalytic routes considered were calculated using the climbing image/nudged elastic band method.[49] The obtained transition states were confirmed after analyzing their vibrational frequencies.

ASSOCIATED CONTENT

Supporting Information

The Supporting Information is available free of charge on the ACS Publications website at DOI: 10.1021/acsnano.9b02052.

Figures S1−S15 and Tables S1−S4 containing further structural analysis, ESI-MS spectrometry, NMR spectroscopy, electrochemical data, and DFT data (PDF)

Crystal structure data (CIF)

AUTHOR INFORMATION

Corresponding Authors

*E-mail: hannu.j.hakkinen@jyu.fi.

*E-mail: nfzheng@xmu.edu.cn.

ORCID

Karoliina Honkala: 0000-0002-3166-1077

Hannu Häkkinen: 0000-0002-8558-5436

Nanfeng Zheng: 0000-0001-9879-4790

Author Contributions

C.S. and N.M. contributed equally to this work.

Notes

The authors declare no competing financial interest.

The CIF data can also be downloaded from the Cambridge Crystallographic Data Centre (CCDC) with access code 1851619.

ACKNOWLEDGMENTS

The experimental work was supported by the National Key R&D Program of China (2017YFA0207302) and the National Natural Science Foundation of China (21731005, 21420102001, 21801212, and 21721001). The computational work at University of Jyväskylä was supported by the Academy of Finland [Grant Nos. 294217 (H.H.), 319208 (H.H.), 277222 (K.H.), and H.H.'s Academy Professorship]. H.H. acknowledges support from China's National Innovation and Intelligence Introduction Base visitor program. S.K. thanks the Väisälä Foundation for a Ph.D. study grant. The computations were made at the CSC center in Espoo, Finland. We thank L. Feng from High-Field Nuclear Magnetic Resonance Research Center (Xiamen University) for the help in the NMR study.

REFERENCES

(1) Goeden, G. V.; Caulton, K. G. Soluble Copper Hydrides: Solution Behavior and Reactions Related to CO Hydrogenation. *J. Am. Chem. Soc.* **1981**, *103*, 7354−7355.

(2) Pirnot, M. T.; Wang, Y.-M.; Buchwald, S. L. Copper Hydride Catalyzed Hydroamination of Alkenes and Alkynes. *Angew. Chem., Int. Ed.* **2016**, *55*, 48−57.

(3) Chen, J.-X.; Daeuble, J. F.; Brestensky, D. M.; Stryker, J. M. Highly Chemoselective Catalytic Hydrogenation of Unsaturated

DOI: 10.1021/acsnano.9b02052
ACS Nano 2019, 13, 5975−5986

Ketones and Aldehydes to Unsaturated Alcohols Using Phosphine-Stabilized Copper(I) Hydride Complexes. *Tetrahedron* **2000**, *56*, 2153−2166.
(4) Bezman, S. A.; Churchill, M. R.; Osborn, J. A.; Wormald, J. Preparation and Crystallographic Characterization of a Hexameric Triphenylphosphine Copper Hydride Cluster. *J. Am. Chem. Soc.* **1971**, *93*, 2063−2065.
(5) Brestensky, D. M.; Huseland, D. E.; McGettigan, C.; Stryker, J. M. Simplified, "One-Pot" Procedure for the Synthesis of $[(Ph_3P)CuH]_6$, a Stable Copper Hydride for Conjugate Reductions. *Tetrahedron Lett.* **1988**, *29*, 3749−3752.
(6) Sanchez, A.; Abbet, S.; Heiz, U.; Schneider, W. D.; Häkkinen, H.; Barnett, R. N.; Landman, U. When Gold Is Not Noble: Nanoscale Gold Catalysts. *J. Phys. Chem. A* **1999**, *103*, 9573−9578.
(7) Yoon, B.; Häkkinen, H.; Landman, U. Interaction of O_2 with Gold Clusters: Molecular and Dissociative Adsorption. *J. Phys. Chem. A* **2003**, *107*, 4066−4071.
(8) Lu, Y.; Chen, W. Sub-Nanometre Sized Metal Clusters: From Synthetic Challenges to the Unique Property Discoveries. *Chem. Soc. Rev.* **2012**, *41*, 3594−3623.
(9) Walter, M.; Akola, J.; Lopez-Acevedo, O.; Jadzinsky, P. D.; Calero, G.; Ackerson, C. J.; Whetten, R. L.; Grönbeck, H.; Häkkinen, H. A Unified View of Ligand-Protected Gold Clusters as Superatom Complexes. *Proc. Natl. Acad. Sci. U. S. A.* **2008**, *105*, 9157−9162.
(10) Tsukuda, T.; Häkkinen, H. *Protected Metal Clusters: From Fundamentals to Appliations*; Elsevier: Amsterdam, 2015.
(11) Jin, R.; Zeng, C.; Zhou, M.; Chen, Y. Atomically Precise Colloidal Metal Nanoclusters and Nanoparticles: Fundamentals and Opportunities. *Chem. Rev.* **2016**, *116*, 10346−10413.
(12) Chakraborty, I.; Pradeep, T. Atomically Precise Clusters of Noble Metals: Emerging Link between Atoms and Nanoparticles. *Chem. Rev.* **2017**, *117*, 8208−8271.
(13) Lopez-Acevedo, O.; Tsunoyama, H.; Tsukuda, T.; Häkkinen, H.; Aikens, C. M. Chirality and Electronic Structure of the Thiolate-Protected Au_{38} Nanocluster. *J. Am. Chem. Soc.* **2010**, *132*, 8210−8218.
(14) Dolamic, I.; Knoppe, S.; Dass, A.; Burgi, T. First Enantioseparation and Circular Dichroism Spectra of Au_{38} Clusters Protected by Achiral Ligands. *Nat. Commun.* **2012**, *3*, 798.
(15) Jadzinsky, P. D.; Calero, G.; Ackerson, C. J.; Bushnell, D. A.; Kornberg, R. D. Structure of a Thiol Monolayer-Protected Gold Nanoparticle at 1.1 A Resolution. *Science* **2007**, *318*, 430−433.
(16) Yang, H.; Wang, Y.; Chen, X.; Zhao, X.; Gu, L.; Huang, H.; Yan, J.; Xu, C.; Li, G.; Wu, J.; Edwards, A. J.; Dittrich, B.; Tang, Z.; Wang, D.; Lehtovaara, L.; Häkkinen, H.; Zheng, N. Plasmonic Twinned Silver Nanoparticles with Molecular Precision. *Nat. Commun.* **2016**, *7*, 12809.
(17) Ren, L.; Yuan, P.; Su, H.; Malola, S.; Lin, S.; Tang, Z.; Teo, B. K.; Häkkinen, H.; Zheng, L.; Zheng, N. Bulky Surface Ligands Promote Surface Reactivities of $Ag_{141}X_{12}(S\text{-}Adm)_{40}^{3+}$ (X = Cl, Br, I) Nanoclusters: Models for Multiple-Twinned Nanoparticles. *J. Am. Chem. Soc.* **2017**, *139*, 13288−13291.
(18) Yang, H.; Wang, Y.; Huang, H.; Gell, L.; Lehtovaara, L.; Malola, S.; Häkkinen, H.; Zheng, N. All-Thiol-Stabilized Ag_{44} and $Au_{12}Ag_{32}$ Nanoparticles with Single-Crystal Structures. *Nat. Commun.* **2013**, *4*, 2422.
(19) Desireddy, A.; Conn, B. E.; Guo, J.; Yoon, B.; Barnett, R. N.; Monahan, B. M.; Kirschbaum, K.; Griffith, W. P.; Whetten, R. L.; Landman, U.; Bigioni, T. P. Ultrastable Silver Nanoparticles. *Nature* **2013**, *501*, 399−402.
(20) Yang, H.; Wang, Y.; Zheng, N. Stabilizing Subnanometer Ag(0) Nanoclusters by Thiolate and Diphosphine Ligands and Their Crystal Structures. *Nanoscale* **2013**, *5*, 2674−2677.
(21) Joshi, C. P.; Bootharaju, M. S.; Alhilaly, M. J.; Bakr, O. M. $Ag_{25}(SR)_{18}^-$: The "Golden" Silver Nanoparticle. *J. Am. Chem. Soc.* **2015**, *137*, 11578−11581.
(22) Jordan, A. J.; Lalic, G.; Sadighi, J. P. Coinage Metal Hydrides: Synthesis, Characterization, and Reactivity. *Chem. Rev.* **2016**, *116*, 8318−8372.
(23) Dhayal, R. S.; van Zyl, W. E.; Liu, C. W. Polyhydrido Copper Clusters: Synthetic Advances, Structural Diversity, and Nanocluster-to-Nanoparticle Conversion. *Acc. Chem. Res.* **2016**, *49*, 86−95.
(24) Liu, X.; Astruc, D. Atomically Precise Copper Nanoclusters and Their Applications. *Coord. Chem. Rev.* **2018**, *359*, 112−126.
(25) Yuan, P.; Chen, R.; Zhang, X.; Chen, F.; Yan, J.; Sun, C.; Ou, D.; Peng, J.; Lin, S.; Tang, Z.; Teo, B. K.; Zheng, L. S.; Zheng, N. Ether-Soluble Cu_{53} Nanoclusters as an Effective Precursor of High-Quality CuI Films for Optoelectronic Applications. *Angew. Chem., Int. Ed.* **2019**, *58*, 835−839.
(26) Cook, A. W.; Jones, Z. R.; Wu, G.; Scott, S. L.; Hayton, T. W. An Organometallic Cu_{20} Nanocluster: Synthesis, Characterization, Immobilization on Silica, and "Click" Chemistry. *J. Am. Chem. Soc.* **2018**, *140*, 394−400.
(27) Edwards, A. J.; Dhayal, R. S.; Liao, P. K.; Liao, J. H.; Chiang, M. H.; Piltz, R. O.; Kahlal, S.; Saillard, J. Y.; Liu, C. W. Chinese Puzzle Molecule: A 15 Hydride, 28 Copper Atom Nanoball. *Angew. Chem., Int. Ed.* **2014**, *53*, 7214−7218.
(28) Chakrahari, K. K.; Liao, J. H.; Kahlal, S.; Liu, Y. C.; Chiang, M. H.; Saillard, J. Y.; Liu, C. W. $[Cu_{13}\{S_2CN^nBu_2\}_6(acetylide)_4]^+$: A Two-Electron Superatom. *Angew. Chem., Int. Ed.* **2016**, *55*, 14704−14708.
(29) Tang, Q.; Lee, Y.; Li, D. Y.; Choi, W.; Liu, C. W.; Lee, D.; Jiang, D. E. Lattice-Hydride Mechanism in Electrocatalytic CO_2 Reduction by Structurally Precise Copper-Hydride Nanoclusters. *J. Am. Chem. Soc.* **2017**, *139*, 9728−9736.
(30) Dhayal, R. S.; Liao, J. H.; Wang, X.; Liu, Y. C.; Chiang, M. H.; Kahlal, S.; Saillard, J. Y.; Liu, C. W. Diselenophosphate-Induced Conversion of an Achiral $[Cu_{20}H_{11}\{S_2P(OiPr)_2\}_9]$ into a Chiral $[Cu_{20}H_{11}\{Se_2P(OiPr)_2\}_9]$ Polyhydrido Nanocluster. *Angew. Chem., Int. Ed.* **2015**, *54*, 13604−13608.
(31) Nguyen, T. A.; Jones, Z. R.; Goldsmith, B. R.; Buratto, W. R.; Wu, G.; Scott, S. L.; Hayton, T. W. A Cu_{25} Nanocluster with Partial Cu(0) Character. *J. Am. Chem. Soc.* **2015**, *137*, 13319−13324.
(32) Stevens, R. C.; Mclean, M. R.; Bau, R.; Koetzle, T. F. Neutron-Diffraction Structure-Analysis of a Hexanuclear Copper Hydrido Complex, $H_6Cu_6[P(p\text{-tolyl})_3]_6$: An Unexpected Finding. *J. Am. Chem. Soc.* **1989**, *111*, 3472−3473.
(33) Zhu, M.; Aikens, C. M.; Hollander, F. J.; Schatz, G. C.; Jin, R. Correlating the Crystal Structure of a Thiol-Protected Au_{25} Cluster and Optical Properties. *J. Am. Chem. Soc.* **2008**, *130*, 5883−5885.
(34) Heaven, M. W.; Dass, A.; White, P. S.; Holt, K. M.; Murray, R. W. Crystal Structure of the Gold Nanoparticle $[N(C_8H_{17})_4][Au_{25}(SCH_2CH_2Ph)_{18}]$. *J. Am. Chem. Soc.* **2008**, *130*, 3754−3755.
(35) Fang, J.; Zhang, B.; Yao, Q. F.; Yang, Y.; Xie, J. P.; Yan, N. Recent Advances in the Synthesis and Catalytic Applications of Ligand-Protected, Atomically Precise Metal Nanoclusters. *Coord. Chem. Rev.* **2016**, *322*, 1−29.
(36) Lopez-Acevedo, O.; Kacprzak, K. A.; Akola, J.; Häkkinen, H. Quantum Size Effects in Ambient CO Oxidation Catalysed by Ligand-Protected Gold Clusters. *Nat. Chem.* **2010**, *2*, 329−334.
(37) Zhang, B.; Sels, A.; Salassa, G.; Pollitt, S.; Truttmann, V.; Rameshan, C.; Llorca, J.; Olszewski, W.; Rupprechter, G.; Bürgi, T.; Barrabés, N. Ligand Migration from Cluster to Support: A Crucial Factor for Catalysis by Thiolate-protected Gold Clusters. *ChemCatChem* **2018**, *10*, 5372−5376.
(38) Hasin, P.; Wu, Y. Sonochemical Synthesis of Copper Hydride (CuH). *Chem. Commun.* **2012**, *48*, 1302−1304.
(39) Fu, M. L.; Issac, I.; Fenske, D.; Fuhr, O. Metal-Rich Copper Chalcogenide Clusters at the Border between molecule and bulk phase: the structures of $[Cu_{93}Se_{42}(SeC_6H_4SMe)_9(PPh_3)_{18}]$, $[Cu_{96}Se_{45}(SeC_6H_4SMe)_6(PPh_3)_{18}]$, and $[Cu_{136}S_{56}(SCH_2C_4H_3O)_{24}(dpppt)_{10}]$. *Angew. Chem., Int. Ed.* **2010**, *49*, 6899−903.
(40) Dhayal, R. S.; Liao, J. H.; Kahlal, S.; Wang, X. P.; Liu, Y. C.; Chiang, M. H.; van Zyl, W. E.; Saillard, J. Y.; Liu, C. W. $Cu_{32}(H)_{20}\{S_2P(OiPr)_2\}_{12}$: The Largest Number of Hydrides Recorded in a Molecular Nanocluster by Neutron Diffraction. *Chem. - Eur. J.* **2015**, *21*, 8369−8374.

DOI: 10.1021/acsnano.9b02052
ACS Nano 2019, 13, 5975−5986

(41) Lemmen, T. H.; Folting, K.; Huffman, J. C.; Caulton, K. G. Copper Polyhydrides. *J. Am. Chem. Soc.* **1985**, *107*, 7774−7775.
(42) Dhayal, R. S.; Liao, J. H.; Lin, Y. R.; Liao, P. K.; Kahlal, S.; Saillard, J. Y.; Liu, C. W. A Nanospheric Polyhydrido Copper Cluster of Elongated Triangular Orthobicupola Array: Liberation of H_2 from Solar Energy. *J. Am. Chem. Soc.* **2013**, *135*, 4704−4707.
(43) Tang, W.; Sanville, E.; Henkelman, G. A Grid-Based Bader Analysis Algorithm Without Lattice Bias. *J. Phys.: Condens. Matter* **2009**, *21*, 084204.
(44) Krabbe, S. W.; Hatcher, M. A.; Bowman, R. K.; Mitchell, M. B.; McClure, M. S.; Johnson, J. S. Copper-Catalyzed Asymmetric Hydrogenation of Aryl and Heteroaryl Ketones. *Org. Lett.* **2013**, *15*, 4560−4563.
(45) Tsai, E. Y.; Liu, R. Y.; Yang, Y.; Buchwald, S. L. A Regio- and Enantioselective CuH-Catalyzed Ketone Allylation with Terminal Allenes. *J. Am. Chem. Soc.* **2018**, *140*, 2007−2011.
(46) Moser, R.; Boskovic, Z. V.; Crowe, C. S.; Lipshutz, B. H. CuH-Catalyzed Enantioselective 1,2-Reductions of alpha,beta-Unsaturated Ketones. *J. Am. Chem. Soc.* **2010**, *132*, 7852−7853.
(47) Zhou, Y.; Bandar, J. S.; Liu, R. Y.; Buchwald, S. L. CuH-Catalyzed Asymmetric Reduction of alpha,beta-Unsaturated Carboxylic Acids to beta-Chiral Aldehydes. *J. Am. Chem. Soc.* **2018**, *140*, 606−609.
(48) Werkmeister, S.; Junge, K.; Beller, M. Copper-Catalyzed Reductive Amination of Aromatic and Aliphatic Ketones with Anilines Using Environmental-Friendly Molecular Hydrogen. *Green Chem.* **2012**, *14*, 2371−2374.
(49) Henkelman, H.; Uberuaga, B. P.; Jónsson, H. A Climbing Image Nudged Elastic Band Method for Finding Saddle Points and Minimum Energy Paths. *J. Chem. Phys.* **2000**, *113*, 9901−9904.
(50) Humphrey, W.; Dalke, A.; Schulten, K. VMD - Visual Molecular Dynamics. *J. Mol. Graphics* **1996**, *14*, 33−38.
(51) *CrysAlisPro*, version 1.171.35.19; Agilent Technologies Inc.: Santa Clara, CA, 2011.
(52) Sheldrick, G. M. SHELXT - Integrated Space-Group and Crystal-Structure Determination. *Acta Crystallogr., Sect. A: Found. Adv.* **2015**, *71*, 3−8.
(53) Dolomanov, O. V.; Bourhis, L. J.; Gildea, R. J.; Howard, J. A. K.; Puschmann, H. OLEX2: A Complete Structure Solution, Refinement and Analysis Program. *J. Appl. Crystallogr.* **2009**, *42*, 339−341.
(54) Sheldrick, G. M. A Short History of SHELX. *Acta Crystallogr., Sect. A: Found. Crystallogr.* **2008**, *64*, 112−22.
(55) Enkovaara, J.; Rostgaard, C.; Mortensen, J. J.; Chen, J.; Dulak, M.; Ferrighi, L.; Gavnholt, J.; Glinsvad, C.; Haikola, V.; Hansen, H. A.; Kristoffersen, H. H.; Kuisma, M.; Larsen, A. H.; Lehtovaara, L.; Ljungberg, M.; Lopez-Acevedo, O.; Moses, P. G.; Ojanen, J.; Olsen, T.; Petzold, V.; et al. Electronic Structure Calculations with GPAW: A Real-Space Implementation of the Projector Augmented-Wave Method. *J. Phys.: Condens. Matter* **2010**, *22*, 253202.
(56) Perdew, J. P.; Burke, K.; Ernzerhof, M. Generalized Gradient Approximation Made Simple. *Phys. Rev. Lett.* **1996**, *77*, 3865−3868.
(57) Walter, M.; Akola, J.; Lopez-Acevedo, O.; Jadzinsky, P. D.; Calero, G.; Ackerson, C. J.; Whetten, R. L.; Grönbeck, H.; Häkkinen, H. A Unified View of Ligand-Protected Gold Clusters as Superatom Complexes. *Proc. Natl. Acad. Sci. U. S. A.* **2008**, *105*, 9157−9162.
(58) Walter, M.; Häkkinen, H.; Lehtovaara, L.; Puska, M.; Enkovaara, J.; Rostgaard, C.; Mortensen, J. J. Time-Dependent Density-Functional Theory in the Projector Augmented-Wave Method. *J. Chem. Phys.* **2008**, *128*, 244101.
(59) Giannozzi, P.; Baroni, S.; Bonini, N.; Calandra, M.; Car, R.; Cavazzoni, C.; Ceresoli, D.; Chiarotti, G. L.; Cococcioni, M.; Dabo, I.; Dal Corso, A.; de Gironcoli, S.; Fabris, S.; Fratesi, G.; Gebauer, R.; Gerstmann, U.; Gougoussis, C.; Kokalj, A.; Lazzeri, M.; Martin-Samos, L.; et al. Quantum Espresso: A Modular and Open-Source Software Project for Quantum Simulations of Materials. *J. Phys.: Condens. Matter* **2009**, *21*, 395502.

DOI: 10.1021/acsnano.9b02052
ACS Nano 2019, 13, 5975−5986